

Residual stress analysis of all perovskite oxide cantilevers

Giuseppe Vasta · Timothy J. Jackson ·
Andreas Frommhold · James Bowen ·
Edward J. Tarte

Received: 4 May 2011 / Accepted: 28 October 2011 / Published online: 19 November 2011
© The Author(s) 2011. This article is published with open access at Springerlink.com

Abstract We have used a method to experimentally determine the curvature of thin film multilayers in all oxide cantilevers. This method is applicable for large deflections and enables the radius of curvature of the beam, at a certain distance from the anchor, to be determined accurately. The deflections of the suspended beams are measured at different distances from the anchor point using SEM images and the expression of the deflection curve is calculated for each cantilever. With this expression it is possible to calculate the value of the radius of curvature at the free end of the cantilever. Together with measured values for the Youngs Modulus, this enabled us to determine the residual stress in each cantilever. This analysis has been applied to $SrRuO_3/BaTiO_3/SrRuO_3$, $BaTiO_3/MgO/SrTiO_3$ and $BaTiO_3/SrTiO_3$ piezoelectric cantilevers and the results compared to two models in which the stresses are determined by lattice parameter mismatch or differences in thermal expansion coefficient. Our analysis shows that the bending of the beams is mainly due the thermal stress generated

during the cooling down stage subsequent to the film deposition.

Keywords Residual stress · Thermal stress · Cantilever · Thin film stress

1 Introduction

There is a wide range of sensors and actuators based on micromachined cantilevers. These devices convert the mechanical vibration of a suspended beam, which may be terminated with a proof mass, into an electrical signal, which may be used to measure acceleration, vibrational frequency or even as a source of electrical power. Usually, the freedom of movement of the cantilever is guaranteed by etching a pit into the substrate and the cantilever is designed so that the curvature is minimized. When a cantilever is fabricated using a multilayer thin film structure, mechanical stresses arise between the layers as a result of a mismatch of lattice constants and thermal expansion coefficients. These result in the beam being curved rather than straight, which is undesirable for some applications. In order to control the curvature of the beam, an understanding of the stresses in the beam is required, which can be obtained from beam theory.

According to beam theory [1], the longitudinal stress in an homogeneous deflected beam, Fig. 1, is:

$$\sigma_x = -\frac{E\delta}{\rho} \quad (1)$$

where E is the Young's Modulus of the beam, δ is the distance from the neutral axis and ρ is the radius of curvature. So the stress varies linearly along the section

G. Vasta (✉) · T. J. Jackson · E. J. Tarte
The University of Birmingham, School of Electrical
Electronic and Computer Engineering, 52 Pritchatts Road,
Edgbaston, Birmingham, B15 2TT, UK
e-mail: pipvast@yahoo.it

A. Frommhold
The University of Birmingham, Nanoscale Physics Research
Laboratory, School of Physics and Astronomy, Edgbaston,
Birmingham, B15 2TT, UK

J. Bowen
The University of Birmingham, School of Chemical
Engineering, Edgbaston, Birmingham, B15 2TT, UK

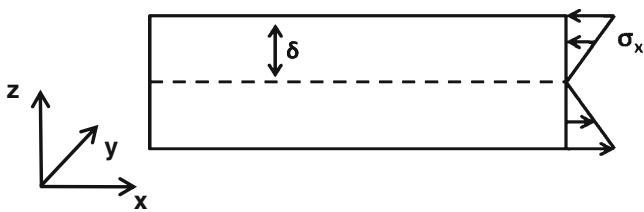


Fig. 1 Longitudinal stress σ_x along the cross section of an homogeneous beam, δ is the distance of a generic fibre from the neutral axis

of the beam. In a multilayer beam, Eq. 1 is valid for each individual layer. The longitudinal stress assumes its maximum value at the bottom and top surface of the cantilever. Previously [2, 3], the radius of curvature ρ of a deflected beam has been evaluated by measuring the deflection δ at the cantilever free end and then the following relation is used:

$$\rho = \frac{L^2}{2\delta} \quad (2)$$

L is the length of the beam. This formula is an approximation valid for small deflections. For larger deflections another method has to be followed. This paper shows a straightforward way to experimentally evaluate the residual stress in released cantilevers and hence determine the residual longitudinal stress in the general case.

We calculated the deflection curve of the cantilever by measuring the deflection of the beam at different distances from the anchor point. This enabled us to evaluate the radius of curvature at the free end of the structure.

The measurement of the deflection profile has been used elsewhere to estimate the curvature of suspended beams containing phase-change materials [4]. In that work the Stoney equation was used to calculate the elastic strain at the interface between a thick cantilever and a thin film grown on its top. Such treatment is only valid if the film thickness is negligible compared with the cantilever thickness [4, 5]. This restriction does not apply to our method and we demonstrate its effectiveness using multilayers to which the Stoney equation would not apply.

In this work the equations of beam theory [1], are used to estimate the residual stress on the top surface of the fabricated cantilevers; we have used this analysis to obtain values for residual stress in all-oxide piezoelectric cantilevers. These consisted of $SrRuO_3/BaTiO_3/SrRuO_3$ and $BaTiO_3/MgO/SrTiO_3$ multilayers which are based on lead free materials and have applications as energy harvesting devices. The use of

an all oxide structure allows the layers to be grown epitaxially, which enables us to exploit the anisotropy of piezoelectric oxides in device design. We found that the first structure can be used to produce energy harvesting devices working in the d_{31} mode because the polar axis is perpendicular to the surface of the film (out of plane), while the second structure can be used for the d_{33} energy harvesting mode [6, 7] as the polar axis is parallel to the surface of the film (in plane). The maintenance of epitaxy throughout the structure requires us to use an oxide sacrificial layer. Residual stress investigations have been also performed on $BaTiO_3/SrTiO_3$ cantilevers, these structures were developed at the beginning of the project to investigate the growing conditions and the properties of such material, however they do not find practical applications as energy harvesting devices.

For the analysed structures, the residual stress produces an upward bending of the beam, after their release. We will show how the application of our stress analysis method enables us to identify the dominant sources of stress in our cantilevers and hence illustrate how it may be applied more generally.

The residual stress in a multilayer beam can be predicted given certain key parameters. We have measured the lattice parameter and Young's modulus for our samples and used these together with published values for Poisson's ratio and thermal expansion coefficients to calculate the residual stress in our samples. We compare these to the stresses determined from the curvature of the beam.

2 Fabrication and characterization of all oxide cantilevers

We used a KrF excimer laser with a wavelength of 248 nm to grow our films by pulsed laser deposition. A 4 Hz pulse repetition rate is used, the distance between the material target and the substrate is set to 5.7 cm and all the devices were fabricated on (001) oriented $SrTiO_3$ substrates.

The first layer grown is $YBa_2Cu_3O_7$ which is used as a sacrificial layer for the release of the beam. This is followed by the $SrRuO_3/BaTiO_3/SrRuO_3$ (out of plane or OP) or the $BaTiO_3/MgO/SrTiO_3$ (in plane or IP) stack. The $BaTiO_3/SrTiO_3$ bilayers (Bi) have been also grown on the top of the sacrificial layer. Our deposition system allows the deposition of only three films in situ, for the Bi structure only three films are necessary so they are grown in situ, for the IP stack first the $MgO/SrTiO_3/YBa_2Cu_3O_7$ tri-layer is deposited followed by a $BaTiO_3/MgO$ bilayer, in the case of the

OP structure first the $BaTiO_3/SrRuO_3/YBa_2Cu_3O_7$ thi-layer is grown followed by a $SrRuO_3/BaTiO_3$ bilayer. The deposition parameters are reported in Table 1.

In these structures, $BaTiO_3$ is the piezoelectric layer, $SrRuO_3$ acts as an electrode for the OP stacks whilst for the IP stacks, the MgO film is introduced to grow the $BaTiO_3$ with the polar axis parallel to the surface of the film, and the $SrTiO_3$ works as buffer layer to improve the interface between the $YBa_2Cu_3O_7$ and the MgO film in the IP structure [8].

The IP structure needs the deposition of a gold top electrode. However the gold deposition is performed at room temperature, so it does not influence the thermal stress analysis which will be developed in the next sections. The cantilever geometry is then defined by contact photolithography and argon ion beam milling. To suspend the beam the sample is undercut in 0.1% HNO_3 , rinsed in distilled water and dried using critical point drying in order to avoid stiction problems.

The Young's modulus of the deposited films has been evaluated using nanoindentation measurements. A NanoTest (Micro Materials, UK) employing a diamond-coated Berkovich indenter has been used, to measure the reduced modulus E_r of the grown films. The reduced modulus E_r is calculated according to the following equation:

$$E_r = \frac{1}{2} \frac{1}{\frac{dP}{dh}} + \frac{\pi^{0.5}}{A_p^{0.5}} \quad (3)$$

dP/dh is the compliance of the contact and A_p is the projected contact area, for a Berkovich indenter:

$$A_p^{0.5} = 4.896h_c \quad (4)$$

h_c is the contact depth and it is equal to:

$$h_c = h_{\max} - 0.75 (h_{\max} - h_r) \quad (5)$$

h_{\max} and h_r are determined from the loading unloading data [9, 10].

Table 1 PLD deposition parameters for the deposited films

Material	Fluence [J/cm ²]	Deposition temperature [°C]	Deposition pressure [Torr]
$YBa_2Cu_3O_7$	3.4	740	0.15 O_2 flow
$SrRuO_3$	3.2	780	0.3 O_2 flow
$BaTiO_3$	3.5	740	0.15 O_2 flow
MgO	3.5	740	0.20 O_2 flow
$SrTiO_3$	3.2	740	0.21 O_2 flow

The Young's modulus is then calculated from the reduced modulus according to the following equation:

$$\frac{1}{E_r} = \frac{(1 - \nu^2)}{E} \frac{(1 - \nu_i^2)}{E_i} \quad (6)$$

E and ν are the Young's modulus and the Poisson's ratio of the specimen under measurements, E_i and ν_i are the same parameters for the indenter, for a Berkovich indenter the Young's modulus E_i is equal to 1141 GPa and the Poisson's ratio is equal to 0.07 [10]. The values of the reduced modulus measured near the top surface of the stack or at the interface between two layers have not been used to calculate the Young's modulus of the grown films. Measurements of the reduced modulus reveal that in the first 10 nm or 15 nm from the top surface of the stack, or from the interface between two layers, the reduced modulus assumes values which are not constant and are not compatible with the bulk Young's modulus of the same material. After the first 10 nm or 15 nm the reduced modulus approaches a value compatible with the Young's Modulus measured in the bulk of the same material; such a value is maintained through the thickness of the film until the next interface is reached.

Indentations were performed from the top surface down to the desired depth through the multilayer. The indenter was held at load for 60 s, then retracted from the sample at a rate of 0.5 nm/s. Each indentation was separated by 50 μ m, to avoid any influence of the previous indentation.

The values reported in Table 2 represent the values of Young's Modulus values averaged over the film thickness over a minimum of 25 measurements. Values obtained from depths near the top surface and near the film interfaces have been rejected, however if such

Table 2 Thermal expansion coefficient, Poisson's ratio and Young Modulus of the deposited films. The Young Modulus has been measured by nanoindentation technique

Material	Thermal expansion coefficient [10 ⁻⁶ 1/K]	Young modulus [GPa]	Poisson ratio
$YBa_2Cu_3O_7$	13.4	129	0.3
$SrRuO_3$	8	190	0.3
$BaTiO_3$ (on MgO or $SrRuO_3$)	11.3	175	0.35
$BaTiO_3$ (on $SrTiO_3$)	11.3	79	0.35
MgO	8	233	0.18
$SrTiO_3$	9.4	130	0.25

values are considered they alter the final value of the Young’s modulus by less than 10%.

X-ray diffraction analysis was performed by using a Siemens D5000 diffractometer. The lattice parameters of the films are reported in Table 3. When the $BaTiO_3$ film is grown on the $SrRuO_3$ layer in the OP stack, the lattice parameters are consistent with the longer polar axis being perpendicular to the surface of the film, this orientation would suit the d_{31} energy harvesting mode. For the IP structures, the in plane lattice parameters are longer than the out of plane ones for $BaTiO_3$ grown on MgO which is consistent with the polar axis being parallel to the surface of the film, this orientation suits the d_{33} energy harvesting mode. In this case the measured polar lattice parameter of 4.002 \AA appears smaller than the bulk value because it is an average value, as there are two possible orthogonal orientations for the polar axis in the plane of the substrate, with the non polar axis lying in the perpendicular direction in plane.

The SEM analysis has been performed with a Philips XL30S FEG. Figure 2 shows SEM pictures of three of the devices under investigation. Figure 1(a) shows a $123 \mu\text{m}$ long, $20 \mu\text{m}$ wide IP U-shape cantilever, the $SrTiO_3$ film is 500 nm thick, the MgO layer is 50 nm thick and the $BaTiO_3$ film is 120 nm thick. Figure 1(b) shows a $234 \mu\text{m}$ long, $20 \mu\text{m}$ wide OP U-shape cantilever, the bottom $SrRuO_3$ layer is 350 nm thick, the $BaTiO_3$ film is 100 nm thick and the $SrRuO_3$ top layer is 50 nm thick. Figure 2(c) shows a $44 \mu\text{m}$ long, $10 \mu\text{m}$ wide Bi cantilver, the $SrTiO_3$ is 500 nm thick and the $BaTiO_3$ is 120 nm thick.

When the cantilever is undercut it leaves a trace on the substrate Fig. 3. The deflection of the beam was evaluated by measuring the distance between the trace on the substrate and the top surface of the cantilever.

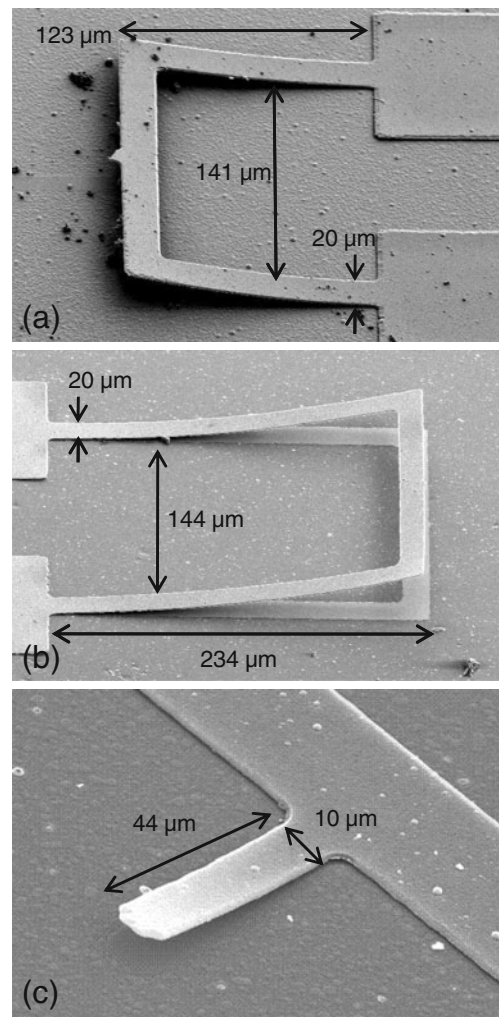


Fig. 2 SEM pictures of: (a) $BaTiO_3/MgO/SrTiO_3$ $123 \mu\text{m}$ long, $20 \mu\text{m}$ wide U-shape cantilever. (b) $SrRuO_3/BaTiO_3/SrRuO_3$ $234 \mu\text{m}$ long, $20 \mu\text{m}$ wide U-shape cantilever. (c) $BaTiO_3/SrTiO_3$ $44 \mu\text{m}$ long, $10 \mu\text{m}$ wide cantilever

Table 3 Lattice constants of the different materials used in the cantilever stack. The lattice parameters have been measured by X-ray diffraction technique

Material	a Measured (a theoretical)	b Measured (b theoretical)	c Measured (c theoretical)
$BaTiO_3$ (on $SrRuO_3$)	3.951 \AA (3.992 \AA)	3.951 (3.992 \AA)	4.069 (4.036 \AA)
$BaTiO_3$ (on MgO)	4.002 \AA	4.002 \AA	3.997 \AA
$BaTiO_3$ (on $SrTiO_3$)	3.996 \AA (3.992 \AA)	3.996 \AA (3.992 \AA)	4.015 \AA (4.036 \AA)
$SrRuO_3$ (on $YBa_2Cu_3O_7$)	5.519 \AA (5.567 \AA)	5.519 \AA (5.530 \AA)	7.825 \AA (7.845 \AA)
MgO (on $SrTiO_3$)	4.220 \AA (4.211 \AA)	4.220 \AA (4.211 \AA)	4.220 \AA (4.211 \AA)

Measurements uncertainties of 300 nm in the y direction and of $1 \mu\text{m}$ in the x direction have been estimated.

To validate the SEM measurements, the deflection of the cantilevers was also measured with a MicroXAM2 interferometer (Omniscan, UK). The interferometer was operated in phase mode employing light of wavelength 510 nm , and at a magnification of $100\times$. Interferograms were found to be unreliable, due to differences in the reflectivities of the various materials. Instead, the interferometer was operated manually, employing a motorised x, y, z stage with $\pm 0.1 \mu\text{m}$ resolution. The interferometric fringes were focused on the sample surface and the position of peak light intensity was considered to be the x, y position of interest, whose position could be determined with approximately

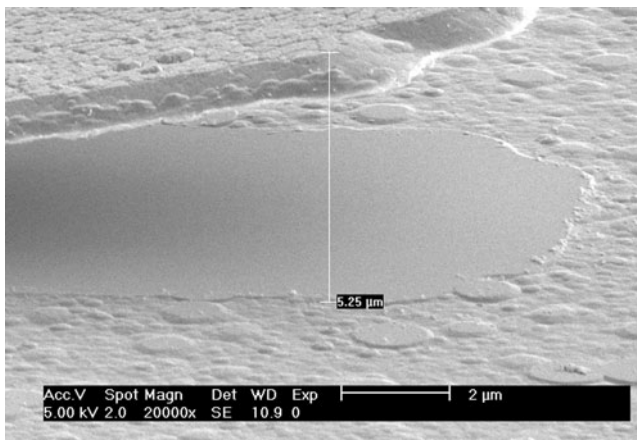


Fig. 3 SEM pictures showing the measurements of the deflection for a $BaTiO_3/SrTiO_3$ cantilever at $32 \mu\text{m}$ from the anchor

$\pm 3 \mu\text{m}$ accuracy due to the manual positioning involved. The corresponding z -position was recorded for each surface location assessed.

3 Analysis of the cantilevers

In order to determine the residual stresses in the cantilevers, we must consider the forces distributed over its cross section. These represent a system equivalent to a couple and the resultant of these forces in the x direction must be equal to zero Fig. 1, [1]. The couple which models the forces along the cross section of the beam generates a moment M . The differential equation describing the deflection curve can be written as:

$$EI_z \frac{d^2y}{dx^2} = -M \tag{7}$$

where I_z is the moment of inertia of the cross section of the cantilever [1]. The deflection of the beam is described by a parabola. The U-shape cantilever is mechanically equivalent to a simple cantilever with a beam width equal to twice the real one [11]. So all the relations for the normal beam can be applied to these devices.

The deflections of three example cantilevers (on three different samples), one for each layer sequence, have been measured at five different distances (A ; B ; C ; D ; E) from the anchors. The data as example of each layer sequence are presented in Table 4. Both the SEM and optical data are shown, together with the equation of the parabola through the first, middle and last points A , C and E respectively. Also shown in Table 4 is the radius of curvature for each

Table 4 Device type, length, width and co-ordinates (x,y) of three example cantilevers (one for each layer sequence); x is the position of the measurement along the cantilever and y is the deflection. The parabolic equations describing the deflection of the cantilevers through the points (A ; C ; E) are reported for both the SEM and the interferometer data, the radius of curvatures of each cantilever calculated from Eq. 8 with the parabola obtained from SEM data are also given

Device	Cantilever type	Length [μm]	Width [μm]	SEM coordinates		Interferometer coordinates		SEM Parabola (Interferometer parabola) $y = ax^2 + bx + c$	Radius of curvature [μm]
				(A ; B ; C ; D ; E) ($x[\mu\text{m}], y[\mu\text{m}]$)	(A ; B ; C ; D ; E) ($x[\mu\text{m}], y[\mu\text{m}]$)				
OP	U-shape	120 μm	20 μm	(0, 1.74); (20, 3.35); (50, 8.44); (90, 19.5); (118, 30.5)	(0, 1.5); (20, 3.5); (50, 8.2); (90, 18); (118, 31)	$y_a = 1620x^2 + 0.053x + 1.74 \cdot 10^{-6}$ $y = 1706x^2 + 0.0487x + 1.5 \cdot 10^{-6}$	403 ± 7.15		
IP	U-shape	120 μm	20 μm	(0, 1.02); (20, 2.3); (50, 5.72); (90, 13.5); (122, 21.6)	(0, 2); (20, 3.6); (50, 5.8); (90, 12.3); (118, 18.6)	$y_b = 1040x^2 + 0.042x + 1.02 \cdot 10^{-6}$ $y = 834x^2 + 0.0343x + 2 \cdot 10^{-6}$	551 ± 37		
Bi	Beam	44 μm	10 μm	(2.33, 1.57); (10, 2.23); (20, 3.2); (30, 4.82); (39, 6.68)	(0, 1.1); (/ , /); (20, 3.4); (30, 4.5); (44, 7.9)	$y_c = 2500x^2 + 0.0339x + 1.51 \cdot 10^{-6}$ $(y = 1650x^2 + 0.082x + 1.1 \cdot 10^{-6})$	217 ± 57		

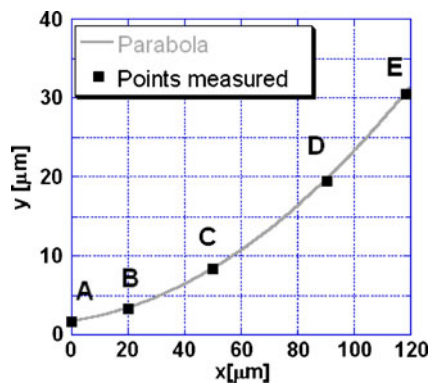


Fig. 4 Parabola and deflection of the measured points for the 120 μm long, 20 μm wide u-shape cantilever having the OP layer sequence

cantilever, calculated from the parabola by using the following expression [1].

$$\frac{1}{\rho} = \frac{\frac{d^2y}{dx^2}}{\left[1 + \left(\frac{dy}{dx}\right)^2\right]^{\frac{3}{2}}} \tag{8}$$

To evaluate the radius of curvature the parabola obtained from the to the SEM data has been considered, this because of the higher resolution associated with the SEM mmeasurements.

The parabola describes the deflection of the cantilevers well, as can be seen from Fig. 4 which shows the parabola and the measured points for the analysed OP device. However it has to be emphasized that Eq. 7 is an approximation [1]. A parabola might not be a good approximation generally, in which case an alternative expression should be considered. For the three example devices the deviations in the measured coordinates of B and D from the parabolic approximation are reported in Table 5. These deviations are in the error range of the SEM coordinates.

As already reported, to validate the method, the deflection of the cantilever has been measured with the interferometer technique. Table 5 also reports the

percentage errors on the parabola coefficients *a* and *b* obtained from the interferometer measurements respect to the parabola coefficients relative to the SEM data. The percentage errors on *a* and *b*, *e_a* and *e_b* respectively, have been calculated from the following expressions:

$$e_a = \left| \frac{a_{SEM} - a_{INT}}{a_{SEM}} \right| \cdot 100 \tag{9}$$

$$e_b = \left| \frac{b_{SEM} - b_{INT}}{b_{SEM}} \right| \cdot 100 \tag{10}$$

where *a_{SEM}* and *b_{SEM}* are the parabola coefficients calculated from SEM data, while *a_{INT}* and *b_{INT}* are the parabola coefficients obtained from interferometer measurements. The coefficient *c* is not considered as its value does not affect the radius of curvature of the cantilevers.

The longitudinal stress at the free end cross section of each of the three example cantilevers is evaluated by using Eq. 1. The value of the Young’s Modulus appropriate for a multilayer system is that of the material with maximum Young’s modulus [1]. In fact in a cantilever system with heterogeneous cross section the width of each layer is normalized to the maximum Young Modulus according to transformed section theory Fig. 5 [1].

To evaluate the longitudinal stress at the cantilever top surface, it is necessary to know the position of the neutral axis in order to calculate the distance between the cantilever’s top surface and the neutral axis itself. The expression for the position of the neutral axis in a *n*-layer film stack is:

$$h_{neut} = \frac{\sum_{i=1}^n (t_i b_{i,c}) h_i}{\sum_{i=1}^n (t_i b_{i,c})} \tag{11}$$

$$b_{i,c} = b_i \frac{E_i}{E_{max}} \tag{12}$$

where *t_i* is the thickness of the layer *i*, *h_i* is the position of the baricenter of the layer *i*, *b_{i,c}* represents the width of the layer *i* normalized to the maximum Young

Table 5 Errors on the points B and D consequence of the parabolic approximation used for the de-fection of the cantilever. Also reported are the percentage errors *e_a* and *e_b* of the parabola coefficients obtained for the interferometers measurements respect to the SEM data. The reported data are relative to the three example devices

Device	Cantilever type	Length [μm]	Width [μm]	Error on B for SEM par. [μm]	Error on D for SEM par. [μm]	<i>e_a</i> SEM-INT	<i>e_b</i> SEM-INT
OP	U-shape	120μm	20μm	+ 0.1	+ 0.22	5.3%	8.11%
IP	U-shape	120μm	20μm	+ 1.22	- 0.28	20%	18.3%
Bi	Beam	44μm	10μm	- 0.13	- 0.04	51.5%	142%

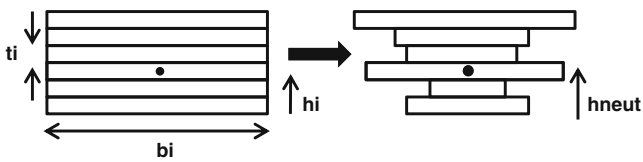


Fig. 5 Equivalent section model of an heterogeneous multilayer cantilever according to the equivalent section theory; b_i is the width of the layer i , t_i is the thickness of the layer i , h_i indicates the position of the baricenter of the layer i and h_{neut} indicates the position of the neutral axis in the equivalent section model

modulus and E_i is the Young Modulus of the layer i , Fig. 5 [12].

The longitudinal stress at the beam top surface for the example OP cantilever is:

$$\tilde{\sigma}_a = -0.104 \cdot 10^9 \pm 0.002 \cdot 10^9 \left[\frac{N}{m^2} \right] \quad (13)$$

for the example IP structure the top surface stress is:

$$\tilde{\sigma}_b = -0.131 \cdot 10^9 \pm 0.009 \cdot 10^9 \left[\frac{N}{m^2} \right] \quad (14)$$

finally for the example Bi device the longitudinal stress at the top surface is:

$$\tilde{\sigma}_c = -0.200 \cdot 10^9 \pm 0.069 \cdot 10^9 \left[\frac{N}{m^2} \right]. \quad (15)$$

These represent the experimental values of the longitudinal stress at the cantilever top surface.

The same analysis has been performed on other cantilevers belonging to the three analysed samples and having the three layer sequences previously reported. The resulting experimental stresses for all the

devices analysed, together with the theoretical values of the longitudinal stresses (which will be discussed in Section 4) are reported in Table 6.

There are three sources of uncertainty in this analysis. The first source is due to the measurement technique and it is linked to the resolution of the measurement instruments. The second is the curve chosen to approximate the deflection of the beam. The third source of error is due to the fabrication process, this kind of error arises from the undercut and resist resolution.

The uncertainties on the values of the residual stresses $\tilde{\sigma}_a$, $\tilde{\sigma}_b$ and $\tilde{\sigma}_c$ have been calculated developing an error analysis on the radius of curvature.

Considering the canonical form of the parabola and Eq. 8, the radius of curvature depends only on the parameters a and b , so the uncertainty in the radius of curvature is dependent on the uncertainty in a and b but not in c .

The radius of curvature of each cantilever was calculated at the free end of the structure, so an error on the length of the cantilever also affects its final value. The principle errors on the cantilever lengths is due to the undercut at the anchors points. Undercuts between 9 μm and 20 μm have been measured.

The uncertainty on the radius of curvature has been evaluated using the following formula:

$$(\Delta\rho)^2 = \left(\frac{\partial\rho}{\partial a} \Delta_a \right)^2 + \left(\frac{\partial\rho}{\partial b} \Delta_b \right)^2 + \left(\frac{\partial\rho}{\partial l} \Delta_l \right)^2 \quad (16)$$

where Δ_a and Δ_b are the standard deviations on the parabola factors a and b , they include the instrument and the fitting error; Δ_l is the uncertainty on the length

Table 6 Experimental stress, theoretical thermal stress and theoretical stress due to combined effect of thermal and misfit stress evaluated at the top surface of each cantilever. For each cantilever the device type corresponding to different layer sequence is indicated, also the cantilever shapes and the cantilever lengths and widths are reported

Device	Cantilever type	Length [μm]	Width [μm]	Experimental stress [10^9 N/m^2]	Theoretical thermal stress [10^9 N/m^2]	Theoretical thermal–misfit stress [10^9 N/m^2]
OP	U-shape	120 μm	20 μm	-0.104 ± 0.002	-0.051	-0.0013
OP	U-shape	128 μm	20 μm	-0.093 ± 0.009	-0.051	-0.0013
OP	U-shape	234 μm	20 μm	-0.051 ± 0.026	-0.051	-0.0013
IP	U-shape	120 μm	20 μm	-0.153 ± 0.011	-0.145	-7.21
IP	U-shape	122 μm	20 μm	-0.131 ± 0.009	-0.145	-7.21
IP	U-shape	180 μm	20 μm	-0.112 ± 0.028	-0.145	-7.21
Bi	Beam	32 μm	10 μm	-0.173 ± 0.136	-0.071	1.2
Bi	Beam	44 μm	10 μm	-0.200 ± 0.069	-0.071	1.2
Bi	Beam	55 μm	10 μm	-0.190 ± 0.112	-0.071	1.2

of the cantilever due to the undercut and to the resolution of the photoresist. The errors on the radius of curvature are reported in Table 4.

The error in the experimental values of the residual stress can be calculated from the error on the radius of curvature, they are reported in Table 6.

4 Theoretical values for the residual stress

Usually vacuum deposited films are in a state of stress. Causes of stress are the mismatch of thermal expansion coefficients between the different layers (thermal stress), the mismatch of lattice constants between the different materials (misfit stress) and the presence of defects in the layers [14]. The theory predicts that an epitaxial layer having a lattice parameter mismatch f with the underneath layer of less than $\approx 9\%$ (as in our case), would grow elastically strained to have the same interatomic spacing of the substrate up to some critical film thickness d_c . Beyond d_c misfit dislocations are introduced. At this point the initially strained film relaxes because the dislocations release the misfit strain. The critical film thickness d_c is expressed by

$$d_c = \frac{b}{8\pi(1+\nu)} \ln\left(\frac{d_c}{b} + 1\right) \tag{17}$$

where ν is the Poisson’s ratio, b is the dislocation Burgers vector and f is the lattice misfit of the film. In a multilayer structure for the layer n grown on the layer $n - 1$ the lattice misfit is defined as

$$f = \frac{a_{n-1} - a_n}{a_n} \tag{18}$$

where a_{n-1} and a_n are the unstrained lattice parameter of the layers n and $n - 1$. A positive f implies that the initial layers of the epitaxial film will be stretched in tension, a negative f means film compression [15]. To calculate the value of d_c for each film present in the two stacks rather than the modulus of the Burger vector, to first approximation it is possible to consider the spacing between the (001) planes of the different crystal structures. The values of the Poisson’s ratios for the grown films are reported in Table 2 [16–20].

By using the measured lattice parameters we have found that for our layer combinations, the critical thickness is less than 10 nm. The film thicknesses in the two stacks are in the order of hundred of nm, this means that only the thermal stress will be considered in the following stress analysis, as the misfit is released by the generated dislocations. Similar considerations have been also reported in [21].

The deposition of the cantilever films is performed at temperatures of 740°C and 780°C, then the film stack is cooled down to room temperature. The thermal stress will be the result of the differences in the film thermal expansion coefficients.

On a rigid substrate the in plane thermal stress in the layer n applied by the layer $n - 1$ can be expressed as

$$\sigma_n = \frac{E_n}{1 - \nu_n} (\alpha_n - \alpha_{n-1})(T_s - T_a) \tag{19}$$

where E_n is the Young modulus, ν_n is the Poisson’s ration, α_n and α_{n-1} are the thermal expansion coefficients of the layers n and $n - 1$, T_s is the temperature during the deposition and T_a is the temperature during the measurement. Thin films can be considered as two dimensional systems. Equation 19 is the two dimensional extension of the relation reported in [22].

When the $YBa_2Cu_3O_7$ is undercut and the beam suspended, the constraint which keeps the multilayer anchored to the substrate is removed. The multilayered structure will bend because of the unbalanced thermal stress present at the film interfaces. Figure 6(a), (b) and (c) show the thermal stresses at the interfaces in the OP, IP and Bi stacks after the $YBa_2Cu_3O_7$ undercutting. Where $\sigma_{SRO1-BTO}$ indicates the stress on the $SrRuO_3$ surface layer applied by the $BaTiO_3$ film. Similar nomenclature applies to the other layers. The thermal expansion coefficients [23–27] the Poisson’s ratio [16–20] and the measured Young Modulus are reported in Table 2.

With these values it is possible to calculate the thermal stress at the interface of each film by using Eq. 19. In the OP multilayer structure each film has to be heated to 780°C during the $SrRuO_3$ deposition, so T_s is chosen equal to 780°C. The temperature during the measurement T_a , is 20°C. In this system the algebraic sum of the thermal stresses at each interface is:

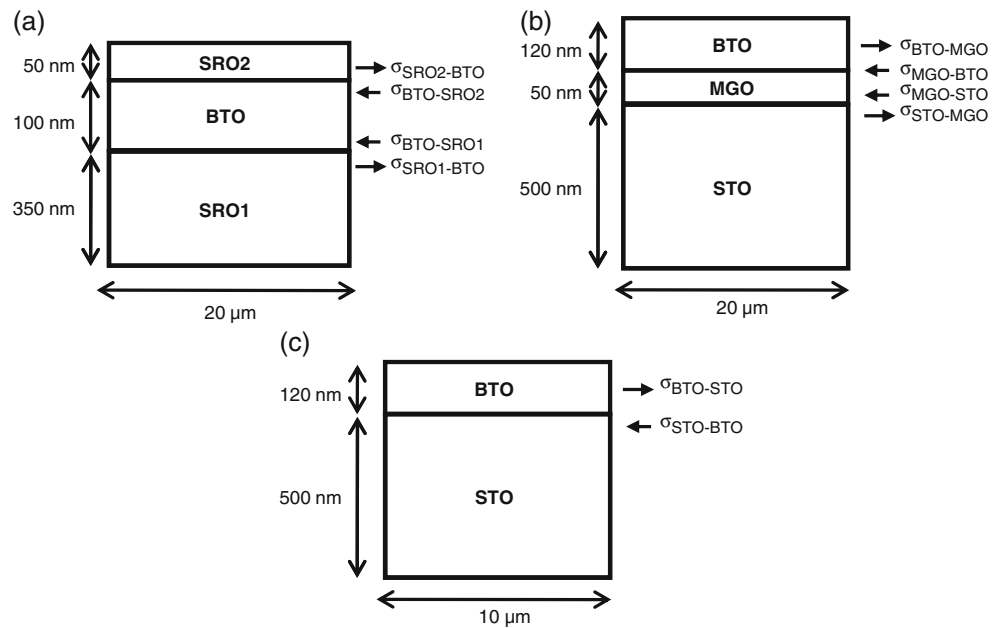
$$\begin{aligned} &\sigma_{SRO1-BTO} + \sigma_{BTO-SRO1} \\ &= \sigma_{BTO-SRO2} + \sigma_{SRO2-BTO} \\ &= -0.0255 \cdot 10^9 \left[\frac{N}{m^2} \right] \end{aligned} \tag{20}$$

the minus sign indicates a compressive stress.

For the IP multilayer system T_s is equal to 740°C and T_a is still 20°C. The algebraic sum of the thermal stresses at each interface is:

$$\sigma_{STO-MGO} + \sigma_{MGO-STO} = -0.111 \cdot 10^9 \left[\frac{N}{m^2} \right] \tag{21}$$

Fig. 6 Longitudinal stress at the interface of each film present in the stack, in (a) $\sigma_{SRO1-BTO}$ indicates the stress on the $SrRuO_3$ surface layer applied by the $BaTiO_3$ film, similar nomenclature applies to the other layers. The arrows indicate if the stress in each layer is compressive (\leftarrow) or tensile (\rightarrow)



for the $SrTiO_3 - MgO$ interface and

$$\sigma_{MGO-BTO}; + \sigma_{BTO-MGO} = -0.034 \cdot 10^9 \left[\frac{N}{m^2} \right] \quad (22)$$

for the $MgO - BaTiO_3$ interface.

In the case of the Bi device, T_s is equal to $740^\circ C$ while T_a is $20^\circ C$, the resulting stress at the $BaTiO_3/SrTiO_3$ interface is:

$$\sigma_{STO-BTO} + \sigma_{BTO-STO} = -0.071 \cdot 10^9 \left[\frac{N}{m^2} \right] \quad (23)$$

the value of the $BaTiO_3$ Young's modulus used for the calculations of the stress at the interface of the Bi structures, as suggested by the indentation measurements, is smaller than that one used for the OP and IP devices. This point is further discussed in Section 5.

According to Eq. 1, the longitudinal stress in each layer varies linearly with the film thickness.

The cantilevers under investigation have total thicknesses of 500 nm and 670 nm, widths between 10 μm and 20 μm and lengths between 32 μm and 230 μm . So at a first approximation it is possible to consider each layer in the stack as a two dimensional system, this means that the stress will occur only at the interfaces.

For the OP system shown in Fig. 6(a) it is possible to assume that the stress at the top surface of the beam is equal to the sum of the stresses at the SRO_2/BTO and at the BTO/SRO_1 interfaces, Eq. 24.

$$\sigma_a = -0.051 \cdot 10^9 \left[\frac{N}{m^2} \right] \quad (24)$$

This is similar in magnitude to the values determined experimentally for the three OP stacks and in excellent agreement with the experimentally determined stress for one of them, Table 6. For the IP stacks, the stress at the top surface of the beam will be equal to the sum of the stresses at the BTO/MGO and at the MGO/STO interfaces, Eq. 25.

$$\sigma_b = -0.145 \cdot 10^9 \left[\frac{N}{m^2} \right] \quad (25)$$

In this case we have excellent agreement with all the experimentally determined values, Table 6.

For the Bi device the stress at the top surface is assumed equal to the stress at the BTO/STO interface:

$$\sigma_c = -0.071 \cdot 10^9 \left[\frac{N}{m^2} \right]. \quad (26)$$

There is a factor 3 between the experimental and the theoretical values, however a large error is present in the experimental stresses and for two devices the theoretical value falls inside the error range, Table 6.

If the contributions coming from the lattice mismatches are considered the stresses at the interfaces of Fig. 6(a) re given by the sum of the thermal stress and of the stress generated by the lattice mismatch. The stress due to the lattice mismatch generated by the layer $n - 1$ on the layer n is:

$$\sigma_{mis.n} = \frac{E_n}{1 - \nu_n} f \quad (27)$$

where f is the lattice misfit defined in Eq. 18.

Considering the algebraic sum of the stresses at the interfaces of the OP stack, the theoretical longitudinal stress at the top surface is:

$$\hat{\sigma}_a = -0.0013 \cdot 10^9 \left[\frac{N}{m^2} \right] \tag{28}$$

this is between five times and one order of magnitude smaller than the experimental values. For the IP devices the introduction of the lattice mismatch in the calculations results in the following top surface stress:

$$\hat{\sigma}_b = -7.21 \cdot 10^9 \left[\frac{N}{m^2} \right] \tag{29}$$

in this case there are two orders of magnitude between experiment and theory. Finally in the case of the Bi cantilevers the contribution of the misfit stress produces the following theoretical value:

$$\hat{\sigma}_c = 1.2 \cdot 10^9 \left[\frac{N}{m^2} \right] \tag{30}$$

also in this case a difference of two orders of magnitude between the experimental and the residual stress is present. Furthermore the positive value of the residual stress at the beam top surface indicates a downward bending of the cantilever, in clear contrast with observations. The values of the residual stress calculated with the contributions of the thermal stress and lattice mismatch are reported in Table 6.

When the contributions of the lattice mismatch are included in the calculation of the residual stress there is a clear disagreement between theoretical and experimental values, this is why the residual stress is mainly attributed to the differences in the thermal expansion coefficients between the materials of the different layers.

5 Discussion

There are two different techniques used to evaluate the residual stress in thin films. In the first method the curvature of a flat substrate is measured after the film deposition and the residual stress is evaluated using the Stoney formula [4, 7, 14, 29].

The assumptions in this method are: the properties of the film-substrate system are such that the film materials contribute negligibly to the overall elastic stiffness; the change in film stress due to substrate deformation is small; the thickness of the film is small compared to the thickness of the substrate and the curvature of the substrate midplane is spatially uniform [5]. Corrections to the original Stoney formula can be made in the case

of films having a thickness which is not negligible with respect to the thickness of the substrate.

Thus the Stoney formula may not accurately describe the bending of our cantilever, for example the radius of curvature of the fabricated cantilevers is not uniform along the length of the beam and furthermore in multilayer cantilevers all the films contribute to the overall elastic stiffness.

When this method is applied to a multilayer structure grown on a certain substrate it is assumed that the individual layers in the film are added sequentially and that the mismatch strain in each layer depends only on the substrate but not on the order in which the layers are formed [5]. To evaluate the stress in a multilayer the substrate curvature has to be measured before and after each layer deposition [5, 7].

All these assumptions can lead to systematic errors in the evaluation of the local residual stresses.

The second technique involves the measurement of the bending of the multilayer structure when all the constraints are removed [14]. This is the method usually used to evaluate the residual stress in released cantilevers. Under the assumption of small deflections, the deflection of the free end is measured [2, 3], and is used to calculate an approximated value for the radius of curvature (Eq. 2). This is only valid for small deflections of the cantilever free end, and so to calculate a more precise value for the radius of curvature, the method which we proposed can be followed. Measurement of the deflections at different distances from the anchor point is a straightforward way to experimentally evaluate the residual stress in multilayers cantilevers.

For the OP devices, one of the experimentally determined residual stress values is in good agreement with the theoretical value and the other two are of a similar order of magnitude. All of the experimentally determined residual stress values for the IP devices agree well with the theoretical value. The level of agreement between experiment and theory may be somewhat fortuitous, since there is more than one value available in the literature for key parameters such as the thermal expansion coefficients of the materials. In particular for *MgO* a different value from that one reported in the table is also found [30].

$$\alpha_{MgO}(300K) = 10.4 \cdot 10^{-6} \left[\frac{1}{K} \right] \tag{31}$$

Assuming this value for the MgO thermal expansion coefficient, the value for the theoretical residual stress at the top surface of the IP device is:

$$\sigma_b = -0.072 \cdot 10^9 \left[\frac{N}{m^2} \right]. \tag{32}$$

In the case of Bi devices the magnitude of the absolute error on the parabolic approximations (error on points *B* and *D*, Table 5) is comparable with the absolute error of the IP and OP structures. The Bi devices experiences deflections which are between three and six times smaller than the deflections experienced by the IP and OP cantilevers, this produces a larger relative error on the parabolic approximation used for the Bi structures. This explains why a bigger error on the residual stress of these cantilevers is present.

For the Bi cantilevers, as already reported in Section 4, the measured value of the Young modulus is smaller than the value measured for $BaTiO_3$ films grown on $SrRuO_3$ or on MgO . This smaller value of 79 GPa is in agreement with that reported in [28]. When the $BaTiO_3$ is grown on MgO or on $SrRuO_3$ its Young's modulus is larger. Further investigation is necessary to understand the origin of such disagreement. It is known that MgO and $SrRuO_3$ are stiffer than $SrTiO_3$ and so an influence of the underlying layer on the Young's modulus of $BaTiO_3$ can not be excluded. Furthermore it has to be highlighted that in the Bi structure all the thin films are deposited in situ while for the IP and OP stacks this is not possible because our deposition system allows the deposition of only three layers in situ. In the IP and OP devices before the deposition of the $BaTiO_3$ the thin film stacks are heated up in oxygen at the deposition temperature and annealed for about 30 minutes before the deposition. The annealing step can improve the quality of the top surface of the film stack which acts as a seed for the $BaTiO_3$ deposition. Alternatively, since it is known that heating and cooling cycles can reduce stresses in ceramics like $BaTiO_3$ [13], stresses in the Bi structures may be higher than those in the IP and OP because the IP and OP structures were grown with extra heating/cooling steps. Thirdly, the Bi structures are smaller than the IP and OP devices so edges effects might contribute to the total longitudinal stress [5].

Nevertheless for two of the Bi structures the theoretical stress lies with the error range of the experimental value. Therefore we consider that the overall agreement with theory is good and that the mismatch between the thermal expansion coefficients is the main cause of the residual stress in these devices. If instead the lattice mismatches are used to calculate the longitudinal stresses at the top surfaces of the cantilevers, there is a difference of one or two orders of magnitude between theoretical and experimental values. This rules out the lattice mismatch as the cause of residual stress.

We believe that the variation in stress values can arise from variations in deposition parameters, associated with the alignment of the laser ablation plume with

the centre of the substrate. For the sample containing the OP structures, two of the devices were much closer to each other than the third device. If the thickness of each layer deposited on the $SrTiO_3$ substrate were not uniform all over the sample, this would give errors in the position of the neutral axis and according to Eq. 1 an error on the value of the residual longitudinal stress.

Another potential source of variation is the value of the Young's modulus. Measurements show that the values of the Young modulus are not constant through the film thicknesses with variations up to 10% around the central value across the thickness of each film. Another source of error might be due to the not perfect undercut in fact it is possible that material from the top part of the sacrificial layer might remain attached to the bottom surface of the cantilever. Finally other sources of stress like microscopic voids, incorporation of impurities and recrystallization [5, 15] could be present in the deposited films.

To validate the method, the measurements of the deflection of the cantilevers have been also performed with the interferometry technique. The measured values together with the corresponding parabola are reported in Table 4. Table 5 reports the percentage errors on the parabola coefficients a and b , e_a and e_b respectively, obtained from the interferometer measurements respect to the parabola coefficients relative to the SEM data. For the IP and OP devices errors on the coefficients between 5% and 20% seem to validate the method applied on the SEM measurements. For the Bi devices errors on the coefficients over 50% are reported, this is attributed to the smaller resolution associated with the interferometer measurements. The Bi devices have lengths between 32 μm and 55 μm and experience a maximum deflection of the free end equal to 10 μm . For these small deflections, the resolution of the method as consequence of the manual measurement involved does not allow the application of the method on these data.

The SEM measurements present a better resolution than the interferometers data, this is why the radius of curvature and the values of the residual stresses at the top surface of the cantilevers have been calculated from the SEM measurements.

6 Conclusions

We have shown a method to experimentally determine the curvature of thin film multilayer suspended cantilever structures. This method is applicable for beams with large deflections and which do not present a constant radius of curvature. It enables the radius

of curvature at a certain distance from the anchor to be determined accurately. The deflection of the suspended beams is measured at different distances from the anchor point using SEM and interferometer images in this way the expression of the deflection curve is calculated for each cantilever. With this expression it is possible to calculate the value of the radius of curvature at the cantilever free end. Together with measured values for the Youngs Modulus, this enabled us to determine the residual stress in a cantilever. This analysis has been applied to $SrRuO_3/BaTiO_3/SrRuO_3$ and $BaTiO_3/MgO/SrTiO_3$ piezoelectric cantilevers. These thin film sequences produce $BaTiO_3$ layers with polar axes oriented out of plane(OP) or in plane(IP) respectively. The OP structures are suited to energy harvesting applications where the d_{31} mode is used whilst the IP structures are suited to the d_{33} mode. Investigations have been also performed on $BaTiO_3/SrTiO_3$ bilayer cantilevers. The results were compared to two models in which the stresses are determined by lattice parameter mismatch or differences in thermal expansion coefficient. The experimentally determined residual stresses of the IP and OP devices were found to agree with the calculated thermal stresses, suggesting that the latter is the source of the curvature, rather than the lattice mismatch. For the Bi structures the experimental stress is three times bigger than the theoretically calculated thermal stress, however in this case a large uncertainty is associated with the experimental values. For energy harvesting applications, the output power of a cantilever increases when its swinging amplitude increases. So in some cases, the bending up, can be used to increase the swinging amplitude of the released beam. In this way it is possible to have swinging amplitudes in the orders of 20 μm without the need to etch the substrate. Using the methods described in this paper, the upward curvature of such cantilevers can be better understood and even tuned by appropriate selection of oxide layers to enhance their performances.

Acknowledgements The Interferometer and Nanoindenter used in this research were obtained, through Birmingham Science City: Innovative Uses for Advanced Materials in the Modern World (West Midlands Centre for Advanced Materials Project 2), with support from Advantage West Midlands (AWM) and part funded by the European Regional Development Fund (ERDF).

This research has been funded by the UK EPSRC under EP/E026494/1 and by The University of Birmingham.

Open Access This article is distributed under the terms of the Creative Commons Attribution Noncommercial License which permits any noncommercial use, distribution, and reproduction in any medium, provided the original author(s) and source are credited.

References

1. S. Timoshenko, *Strength of Materials*, (D. Van Nostrand Company Inc., USA, 1955), pp. 92–97, 136–140, 210–226
2. H. Lakdawala, G.K. Fedder, Analysis of temperature-dependent residual stress gradient in CMOS micromachined structures. *Transducers '99*, 526–529 (1999)
3. J.S. Pulskamp, A. Wickenden, R. Polcawich, B. Piekarski, M. Dubey, Mitigation of residual film stress deformation in multilayer microelectromechanical systems cantilever devices. *J. Vac. Sci. Technol., B*, **21**(6), 2482–2486 (2003)
4. J.A. Kalb, Q. Guo, X. Zhang, Y. Li, C. Sow, C.V. Thompson, Phase-change materials in optically triggered microactuators. *Journal of Microelectromechanical System* **17**(5), 1094–1103 (2007)
5. L.B. Freund, S. Suresh, *Thin Film Materials*, vol. 88 (Cambridge University Press, 2003), pp. 93–95, 125–127
6. W.J. Choi, Y. Jeon, J.H. Jeong, S.G. Kim, Energy harvesting MEMS device based on thin film piezoelectric cantilevers. *J. Electroceram.* **17**, 543–548 (2006)
7. Y.B. Jeon, R. Sood, J.H. Jeong, S.G. Kim, MEMS power generator with transverse mode thin film PZT. *Sens. Actuators, A*, **122**, 16–22 (2005)
8. G. Vasta, T.J. Jackson, J. Bowen, E. Tarte, New Multilayer Architectures for Piezoelectric $BaTiO_3$ cantilever systems. *MRS Proceedings*, 1325, mrrs11-1325-e08-05 (2011). doi:10.1557/opl.2011.970
9. A.C. Fischer-Cripps, *Nanoindentation* (2nd edn. Springer, New York, 2004), pp. 6–45
10. Micro Materials Ltd. (MML NanoTest manual 2004)
11. L. Latorre, P. Nouet, Y. Bertrand, P. Hazard, F. Presseccq, Characterization and modeling of a CMOS-compatible MEMS technology. *Sens. Actuators* **74**, 143–147 (1999)
12. S. Baglio, S. Castorina, N. Savalli, *Scaling Issues and Design of MEMS*. (John Wiley & Sons LTD, England, 2007)
13. Y. He, Heat capacity thermal conductivity and thermal expansion of barium titanate-based ceramics. *Thermochim. Acta* **419**, 135–141 (2004)
14. S. Huang, X. Zhang, Gradient residual stress induced elastic deformation of multilayer MEMS structures. *Sens. Actuators, A*, **134**, 177–185 (2007)
15. M. Ohring, *The Materials Science of Thin Films* (Academic Press, London, 1992), pp. 314–319
16. E. Bartolome, J.J. Roa, B. Bozzo, M. Segarra, X. Granados, Effective silver-assisted welding of YBCO blocks: mechanical versus electrical properties. *Supercond. Sci. Technol.* **23**, 045013 (6pp) (2010)
17. K. Khamchame, Thesis: Ferroelectric Heterostructures Growth and Microwave Devices. Department of Microelectronics and nanoscience, (Chalmer University of Technology, Goteborg, 2003)
18. A.C. Dent, C.R. Bowen, R. Stevens, M.G. Cain, M. Stewart, Effective elastic properties for unpoled barium titanate. *J. Eur. Ceram. Soc.* **27**, 3739–3743 (2007)
19. C.S. Zha, H.K. Mao, R.J. Hemley, Elasticity of MgO and a primary pressure scale to 55 GPa. *PNAS* **97**(25), 13494–13499 (2000)
20. T. Suzuki, Y. Nishi, M. Fujimoto, Defect structure in homoepitaxial non-stoichiometric strontium titanate thin films. *Philos. Mag., A*, **80**(3) 621–637 (2000)
21. I.B. Misirlioglu, S.P. Alpay, F. He, B.O. Wells, Stress induced monoclinic phase in epitaxial $BaTiO_3$ on MgO . *J. Appl. Phys.* **99**, 104103 (2006)
22. J.A. Thornton, D.W. Hoffman, Stress related effects in thin films. *Thin Solid Films* **171**, 5–31 (1989)

23. AZoM.com, Strontium Titanate (SrTiO₃) - properties and applications, (2004) <http://www.azom.com/Details.asp? ArticleID=2362>. Accessed 5 November 2011
24. J. Kawashima, Y. Yamada, I. Hirabayashi, Critical thickness and effective thermal expansion coefficient of YBCO crystalline film. *Physica C*, **306**, 114–118 (1998)
25. S.N. Bushmeleva, V.Y. Pomjakushin, E.V. Pomjakushina, D.V. Sheptyakov, A.M. Balagurov, Evidence for the band ferromagnetism in *SrRuO₃* from neutron diffraction. *J. Magn. Mater.* **305**, 491–496 (2006)
26. Y. He, Heat capacity thermal conductivity and thermal expansion of barium titanate-based ceramics. *Thermochim. Acta* **419**, 135–141 (2004)
27. SPI supplies, SPI Supplies Brand MgO Magnesium Oxide Single Crystal Substrates, Blocks, and Optical Components, (1999) <http://www.2spi.com/catalog/submat/magnesium-oxide.shtml>. Accessed 5 November 2011
28. B.L. Cheng, M. Gabbay, G. Fantozzi, W.J. Duffy, Mechanical loss and elastic modulus associated with phase transitions of barium titanate ceramics. *J. Alloys Compd.* **211/212**, 352–355 (1994)
29. Z. Feng, E.G. Lovell, R.L. Engelstad, A.R. Mikkelsen, P.L. Reuand Jaewoong Sohn, Film stress characterization using substrate shape data and numerical techniques. *Mat. Res. Soc. Symp. Proc.* **750**, Y.3.4.1–Y.3.4.6 (2003)
30. O. Madelung, U. Ressler, M. Schulz, Magnesium oxide (MgO) crystal structure, lattice parameters, thermal expansion. The Landolt-Brnstein Database (<http://www.springermaterials.com>), doi:10.1007/10681719_206. vol. III/17B– 22A–41B SpringerMaterials